DRAL
Daresbury Laboratory
Rutherford Appleton Laboratory

RAL Report
RAL-94-076

The GAJET Experiment at the LHC

P D Dauncey T Nakada and J -P Perroud

July 1994

Rutherford Appleton Laboratory Chilton DIDCOT Oxfordshire OX11 0QX

IPNL 94-2
PSI-PR-94-23
RAL-94-076

The GAJET Experiment at the LHC

The GAJET Collaboration

Presented by

P. D. Dauncey[1], T. Nakada[2] and J.-P. Perroud[3]

19 July 1994

1) Rutherford Appleton Laboratory, Didcot, Great Britain
2) Paul Scherrer Institute,Villigen, Switzerland
3) University of Lausanne, Lausanne, Switzerland

Presented at "Beauty 94", The 2nd International Workshop on B-Physics at Hadron Machines, 24-29 April 1994, Le Mont Saint Michel, France.

1 Introduction[1]

The standard model is undoubtedly the most successful theory in particle physics. It has passed almost all the experimental tests up to now. Clearly, a theory beyond must include the standard model as its low energy limit in order to be able to explain the observed phenomena.

CP violation is one of few remaining phenomena which possibly may not be accommodated in the framework of the standard model. Although experiments with kaons will still dominate the scene for a while, the B-meson system provides the cleanest ground to test whether observed violation of CP symmetry is a sign of new physics or not.

By the time LHC will become fully operational, a CP violation effect in the theoretically cleanest and experimentally simplest decay mode $B^0 \to J/\psi K_S$ could well have already been seen elsewhere, for example at e^+e^- B-meson factories, by HERA-B and at FNAL [1]. Therefore, the aim of a dedicated B experiment at LHC must be to make precision measurements of all the three angles of the unitarity triangle. This requires the reconstruction of B-meson decays such as $B^0 \to \pi^+\pi^-$ or DK and $B_s \to D_s\pi$ or D_sK. The decay modes which are expected to exhibit very small CP asymmetries in the standard model, such as $B_s \to J/\psi\,\phi$ are also of great interest [2].

This requires a detector capable of identifying particles up to a high momentum, measuring accurately the decay time of the B-meson and triggering on various B-meson decay modes into a few charged particles. In order to realise such an experiment at the LHC, we chose a technique using an internal gas jet target (GAJET). In this paper, we discuss the reason of this choice, the proposed spectrometer, the trigger and the expected physics performance of the experiment.

2 Choice of the Method

Experiments using collider mode at LHC have a clear advantage over those using fixed target mode in the b-quark production rate; i.e. ~ 500 times larger b-quark production cross section and ~ 100 times larger $\sigma_{b\bar{b}}/\sigma_{\rm total}$.

On the other hand, the fixed target mode has an obvious advantage in the acceptance. Due to the large longitudinal boost in fixed target mode, a forward spectrometer with a polar angle coverage of less than 100 mrad gives close to 100% acceptance for the B-meson decay final states. It can be shown that the b-quark cross section advantage in collider mode is reduced from a factor of ~ 500 to ~ 8 [3] due to this effect.

A further reduction of this factor may exist in the first level trigger. The first level trigger is a challenge to all the LHC experiments. This is particularly difficult for experiments measuring CP violation in B-meson decays. Signatures for events with B-meson decays are

1. Particles with a large transverse momentum, p_T, due to the large B-meson mass, particularly charged leptons.

2. Particles with a large impact parameter with respect to the primary vertex due to the long B-meson lifetime.

In a fixed target experiment using a point-like target, these two characteristics can be fully exploited in the first level trigger.

Figures 1 and 2 show the p_T spectra of the charged hadron with the largest p_T of the event (leading p_T hadron) for minimum bias events and $b\bar{b}$ events where one of the b quarks hadronises to a neutral B-meson which then decays into $\pi^+\pi^-$ for the fixed target case (figure 1) and for the collider case (figure 2). The acceptances for the both experiments are restricted to 3.5-87 mrad and 10-600 mrad in the polar angle respectively. The luminosities are assumed to be 2×10^{33} cm^{-2}s^{-1} for the fixed target case and 3.8×10^{32} cm^{-2}s^{-1} for the collider case. It shows that the hadronic p_T trigger has a rejection of $\sim 10^{-4}$ against minimum bias events in fixed target mode while it is only $\sim 10^{-2}$ in collider mode for the same $b\bar{b}$ event efficiency of 0.8 if the true p_T can be used.

[1] Presented by T. Nakada

The electron large p_T trigger in collider mode is also difficult due to many γ's from π^0 decays resulting in $e^{\pm}$ from conversions. In the minimum bias events, the average multiplicity of π^0 in one bunch crossing for fixed target mode is about $\sim 1/3$ of that for collider mode with the same angular acceptances and luminosities discussed above. The p_T spectra of π^0 in the minimum bias events are harder for collider mode than fixed target mode as seen from figure 3.

Thus, a first level trigger based on calorimetry, which can be made very fast, for hadrons and electrons provides the effective suppression of minimum bias events in fixed target mode in addition to the large p_T muon trigger which is standard to all the LHC experiments. The large p_T lepton trigger is mainly sensitive to the semi-inclusive B$\rightarrow$ J/ψX decays and the semileptonic B-meson decays which are used to tag the flavour of the other B-mesons. The large p_T hadron trigger becomes useful for self-tagging modes like $K^{\pm}\pi^{\mp}$ and Dπ.

An impact parameter trigger requires the reconstruction of tracks in the vertex detector where the particle density is high and is difficult to implement as a first level trigger. If the target is point-like, the selection of events associated with tracks having large impact parameters becomes simpler. One method is to use an optical discriminator (section 4.1.1). The other is to use a vertex detector system made of pixels with a pointing r-ϕ geometry as shown in figure 4. With this geometry, each track coming from the primary vertex and nearby vertices is confined to the same ϕ sector of the three planes. The average track multiplicity in one ϕ sector is less than one. In such a case, readout of the hit can be made very fast and the track pattern recognition can be simplified due to the absence of the combinatorial background. Ghost tracks due to spurious hits are negligible since a track requires a triple coincidence in the same ϕ sector. Track finding can be done in parallel for different ϕ sectors which speeds up the trigger decision.

The pixel division along the r direction is made in such a way that all the tracks from the primary vertex hit pixels with the same r address. Tracks from downstream of the primary vertex, which is a signature for the tracks from B and D decay vertices, produce hits with increasing r addresses for increasing plane numbers. Therefore, a very simple algorithm can be implemented to look only for track candidates from B and D decays. The difference in the r addresses of the hits in the first and the last planes measures the impact parameter of the track. With such a vertex detector system, it is possible to calculate the number of tracks with positive non-zero impact parameters within 1 μs, as well as the values of impact parameters which can be used to form a trigger decision. The expected performance of the combined system of the optical discriminator and the vertex detector is discussed in section 4.

It is important to minimise any material around the primary vertex which could produce conversions and interactions of the primary tracks. Tracks from those conversions and interactions are recognised as tracks with a large impact parameter by the vertex trigger system. Here, the smaller average multiplicity of one interaction for fixed target mode compared with collider mode is an additional advantage.

An internal gas jet target provides a priori known primary vertices from the point-like source. The transverse dimension of the primary vertex is given by the transverse beam size which is sufficiently small. The longitudinal size of the gas jet can be made to be $\sigma \approx 1$ mm.

Due to these reasons, we believe that an experiment using the internal gas jet target at LHC can compete well with an experiment designed to work in collider mode. The first level trigger is effective, flexible and robust since it uses different characteristics of the B-meson event. The internal gas jet target has an additional advantage that it is a well proven technique and has been shown to be compatible with the operation of the collider. The luminosity can be increased significantly by using heavy gas.

3 The GAJET Detector

Figure 5 shows the GAJET detector which is described in detail elsewhere [4]. The gas jet target is followed by the optical discriminator, vertex detectors, tracking planes and a RICH. The position of the RICH is given by the beam pipe radius and a minimum acceptance of $\theta = 3.5$ mrad.

The RICH is followed by planes of tracking chambers with a magnet in between, by a transition radiation detector and by electromagnetic and hadronic calorimeters. The last component of the detector is the muon system. We place the RICH in front of the magnet in order to maximise the K_S decay region for the $B^0 \rightarrow J/\psi K_S$ decays. This also minimises the distance between the magnet and the calorimeters. Since the transverse energy trigger ignores the magnetic bending of the track, this distance should be kept as small as possible.

3.1 Gas Jet

We intend to use a hydrogen cluster jet which is similar to one used in the UA6 experiment [4]. A minor modification will make the length of the cluster along the beam 2 mm with a higher gas density than that of UA6 giving the same integrated thickness of 4×10^{14} atoms/cm^2. With the nominal LHC beam current of 850 mA, the resulting luminosity is 2×10^{33} cm^{-2}s^{-1}. This corresponds to an average of three interactions in one bunch crossing and produces 2×10^3 $b\bar{b}$ pairs per second assuming $\sigma_{b\bar{b}} = 1$ μb.

The gas density of the target cannot be further increased. Thus, we propose to use Ar (A=40) gas if the beam current is much lower than the nominal one in the initial stage of the LHC running [5]. Since the b-quark production cross section is expected to increase approximately linearly with A, 40 times more $b\bar{b}$ pairs can be produced with the same luminosity. Using this Ar gas jet target, B-meson production rates of 2×10^3 $b\bar{b}$ pairs per second could be obtained even at the initial stage of the LHC running.

3.2 Optical Discriminator

This is discussed fully in the trigger section 4.1.1.

3.3 Vertex Detector

The vertex detector shown in figure 4 consists of two systems, one covering a polar angle of 17.5 to 87 mrad and the other 3.5 to 17.5 mrad. In order to keep the radiation damage to an acceptable level, the Si detector must be placed at least 7 mm away from the beam. The first plane of the first system is 40 cm away from the interaction point and the second system 200 cm. We expect to replace the vertex detector twice a year.

Each system consists of five super-planes of Si strip detectors. Each super-plane has two planes of Si strip detectors giving accurate x and y coordinates. Double-sided silicon detectors have not been considered for the moment since they are known to be less resistant to radiation damage.

There are, in addition, three pixel planes placed closely to the strip planes. They are used for the trigger as explained in the previous section. They will be also used for pattern recognition off-line. As explained in the previous section, no ghost track is expected due to their r-ϕ pointing geometry. Once tracks are reconstructed in space, hits on the strip detectors can be associated to the track with very high efficiencies. As a result, we do not need more than five strip super-planes in the each system.

3.4 Roman Pot

The optical discriminator and both the vertex detector systems must be placed in the Roman pots so that they can be retracted away from the beam during the time of injection [6]. The wall of the pot will be made in a pointing geometry so that particles from the interaction point with a polar angle between 3.5 and 87 mrad do not traverse too much material.

3.5 Particle Identification

A ring imaging Cherenkov counter (RICH), using a mixture of He and CF_4 as a radiator, and a transition radiation detector (TRD) will be used for particle identification. For K/π separation,

the RICH can be used for momenta from 10 to 260 GeV and the TRD will be used from 150 up to 450 GeV. The overlapping momentum region is used to inter-calibrate the two detectors.

Using He as a radiator, it is in principle possible to do K/π separation up to $\sim$ 400 GeV only with the RICH. However, such a RICH has to be very long (more than 10 m long) in order to obtain a large enough number of photons. This introduces a difficult construction problem and we exclude this solution.

3.6 Momentum Analyser

A dipole magnet and sets of honeycomb strip chambers (HSC) will be used to analyse the momentum of the charged track. The 1 Tesla magnet provides 4 Tm and the spatial resolution of the tracking system is expected to be < 100 μm. This combination gives a sufficient momentum resolution, $\sigma_p/p < 10^{-4} \times p$ (p in GeV), so that the $B \rightarrow \pi^{\pm}\rho^{\mp}$ decay can be separated from $B \rightarrow \pi^+\pi^-$ using the $\pi^+\pi^-$ invariant mass only.

3.7 Calorimeters

Both electromagnetic and hadronic calorimeters use sandwiches of scintillator and Pb (electromagnetic) or Fe (hadronic) plates. There is also a pre-shower counter ($\sim$ 2 radiation lengths) in front of the electromagnetic calorimeter. Combination of the three gives online identification of γ, $e^{\pm}$ and hadrons. Calorimeters are used in the first level transverse energy trigger. In offline analysis, the calorimeters are used to identify $e^{\pm}$ and have an e/hadron rejection of 10^{-3}.

3.8 Muon System

The muon system consists with 1 m thick iron followed by the three tracking planes. Tracking system uses mainly HSC, which are also used as the main tracking system. The signal from HSC is not fast enough to be used in the first level trigger. Therefore, we added resistive plate chambers (RPC) and parallel plate chambers (PPC) for the first level trigger. PPC are used only in the small region close to the beam where the rate is high. The muon system gives a μ/hadron rejection of 10^{-3}. Note, these numbers are for the actual particles entering the relevant detector system, so decays in flight and overlapping tracks degrade these rejection factors to $\sim 5 \times 10^{-3}$

4 Triggering[2]

At our design luminosity, each proton bunch leads to interactions in the target. The purpose of the first level trigger is to bring the 40 MHz event rate associated with the 25 ns LHC bunch separation to below 50 KHz compatible with second level trigger or with a further event analysis by a processor farm. The data acquisition system will have an architecture very similar to that proposed for the large LHC/SSC experiments.

Since the front-end electronics, which will become standard in a few years, is usually designed to provide a pipeline depth of 64 or 128 events, the decision time of the first level trigger should be less than 1.6 μs or 3.2 μs and should have no dead-time. Furthermore, the first level trigger should be robust, redundant and tunable during the experiment.

To achieve these goals, the first level trigger in the GAJET experiment is based on two types of independent physics characteristics which can distinguish minimum bias events from interesting B events; the events which contain tracks with large impact parameters (with an origin displaced downstream of the target) and tracks with large p_T are selected (see section 2).

[2]Presented by J.-P. Perroud

4.1 Impact parameter first level trigger

For the impact parameter trigger we propose two fast components; an optical discriminator which discriminates events, within a few ns, according to the sum of the impact parameters of associated charged tracks and a set of homothetical pixel silicon detectors sensitive to the displaced secondary vertices. These two components are clearly correlated and are best discussed as a whole. Both components have a pointing geometry and make full use of the point-like target.

4.1.1 Optical Trigger

The optical discriminator [7] consists of a portion of a spherical crystal shell centered on the middle of the production target as shown in figure 6. A fast photodetector at the edge of the crystal detects only those Cherenkov photons produced in the crystal by a charged particle having an impact parameter with respect to the center of the target larger than a threshold value $b_{\min}$. The response time is of the order of a few ns.

The quantity $b_{\min}$ depends only on the crystal properties and can be tuned. By denoting n_1 and n_2 to be the refractive indexes of the crystal and the surrounding media, the threshold of the device is given by [8]:

$$b_{\min} = \epsilon\, R/2n_2$$

where R is the radius of the crystal sphere and ϵ is the achromaticity parameter defined as

$$n_1^2 - n_2^2 = 1 - \epsilon$$

which has to be positive and close to 0. For a single crystal with $n_1 = \sqrt{2}$ surrounded by air or vacuum, we obtain $\epsilon = 0$.

Feasibility studies of the idea were performed during 1992 at Fermilab [9] using a flat MgF_2 crystal and at CERN [8] with a R=100 mm radius spherical shell of LiF which was 3 mm thick and had an aperture of 60 mm. The results are very encouraging. The crystal appears as a fast and tunable impact parameter band selector. The lower level of the band is adjusted by an appropriate choice of the parameter ϵ defined above and the upper level by collimation of the output light. Figure 7 shows the collected signal, obtained with a photomultiplier, as a function of the impact parameter of the incident charged particle. The measured shape is in good agreement with simulations. For small impact parameters, the background level is quite low, of the order of a few percent. The average number of photoelectrons for impact parameters below 2 mm is however still too low to achieve a high efficiency to trigger B-mesons events.

A research and development program is in progress at CERN [10] to improve the results obtained so far with the LiF crystal on the threshold and slope of the response signal. A solution for the threshold has already been found and is reported in detail [11] at this conference. The refractive indexes (and hence also the achromaticity ϵ and $b_{\min}$) are wavelength dependent. With a single medium, a quasi-achromatic behaviour cannot be obtained. However, if the crystal is constructed with a core of a high index material and a cladding of an appropriate lower index material, the wavelength dispersion of the core material may be balanced by the dispersion of the cladding material giving an achromatic pair. This is the case for a sapphire core with a Cargille liquid cladding.

To improve the slope of the response one can use, instead of a photomultiplier (average quantum efficiency of less than 20% in the 200 to 500 nm wavelength range), the very promising VLPC's [12] with a much higher quantum efficiency of 55% in the 400 to 800 nm range.

A further improvement in the slope can be obtained by replacing the single shell by several sub-shells keeping the total thickness to be the same. For small impact parameters, the photoelectron yield is then approximately multiplied by the number of sub-shells.

We have simulated the response of a 6 layer sapphire device with an external radius of curvature of 100 mm and a diameter of 60 mm. Each layer has a thickness of 0.3 mm and the 0.1 mm spaces in between the two layers are filled with the cladding made of Cargille liquid at the temperature of 26 degrees. The total thickness of the device corresponds to the 0.45% of an interaction length and

2.2% of a radiation length. A central hole, 3 mm in diameter, allows the beam to pass through. The angular acceptance coverage is from 15 to 300 mrad.

The assumed luminosity is $2 \times 10^{33}\text{cm}^{-2}\text{s}^{-1}$ with a luminous region which has a transverse width of 0.05 mm and a longitudinal size along the beam direction of 1 mm.

As a photodetector, we assume VLPC's coupled to the crystal through optical fibers with double cladding and large acceptance. The simulation takes into account various effects including pile-up of events, multiple scattering, photon conversion, nuclear interactions and delta-ray production in the crystal.

Figure 8 shows the photoelectron yield for a particle crossing the crystal as a function of its impact parameter. The flat background contribution of ~ 0.09 photoelectrons shown by the open circles essentially results from nuclear interactions and delta-ray production upon which an extra contribution of 0.02 photoelectrons was added to take into account a possible scintillation in the sapphire or in the cladding liquid. The signal rises up to 10 photoelectrons for impact parameters less than 1 mm and then saturates. For an impact parameter of 0.5 mm we observe a yield of about 4 photoelectrons.

Figure 9 shows the normalised distributions of the number of photoelectrons per event for B$\rightarrow \pi^+\pi^-$ events and for minimum bias events. For a threshold in the number of photoelectrons of 10, 80% of the B$\rightarrow \pi^+\pi^-$ events are retained and only 10% of the minimum bias events. A device with a radius of 300 mm and a hole of 2 mm in diameter would be less sensitive to the impact parameter (sensitivity is inversely proportional to R) but the increase in angular coverage at small angles, 3.3 mrad to 100 mrad, provides a better overall performance.

Since the optical discriminator works very fast (a few ns), it can be used as a first level trigger. It provides a reduction of minimum bias events by a factor of ~ 10 with a B-events efficiency of $\sim 70\%$. We are currently studying the possibility to take advantage of the high granularity of the VLPC photodetector. Since we can expect an average of more than 4 photoelectrons for a single particle with an impact parameter greater than 0.5 mm, an improvement of a further factor of 10 in the reduction of minimum bias events by fast topological criteria may be possible.

4.1.2 Vertex Detector

As already mentioned in section 2, we propose to use two systems where each consists of three r-ϕ silicon pixel planes for the first level trigger. Each plane is segmented into 32 ϕ-sectors. Within a sector, the radial size of the pixel increases with the distance from the plane to the gas jet and with its radial position. This is done in such a way that the pixels belonging to the same sector and with same r-addresses in the three planes of a system are exactly homothetical relative to the center of the target. Particles from the primary vertex, located inside the point-like target, fire pixels in the same ϕ-sector and with the same r-addresses. Particles originating from a secondary vertex located downstream of the target fire pixels in the same ϕ-sector but with increasing r-addresses. The difference Δ in r-addresses between the last and first plane gives an estimate of the z-coordinate of the intercept of the track with the beam axis. The intermediate plane is used just to check that the three pixels are actually on a straight line. The scale of the radial pixel size is chosen to provide a given resolution in the z-coordinate which is 2.2 mm for system I and 11.3 mm for system II. The number of pixels in each sector has been chosen to be 564.

The trigger algorithm becomes very simple. Firstly, hits with a r-address difference Δ less than 2 are masked in each ϕ-sector. If a combination of three aligned hits with $\Delta \geq 2$ is found from the remaining hits in one sector, the number of candidate secondary vertex tracks N_{si} is incremented by one unit. Note also that one can update other parameters such as Σ, the sum of the Δ for each candidate track, at the same time.

The average numbers of tracks seen by the silicon detector at our nominal luminosity is about 30 for B-events and about 18 for minimum bias events. The probability to have two tracks originating from displaced secondary vertices in the same ϕ sector is only about 2%. The pixel occupancy is less than 0.2%. Thus, the pattern recognition is simple and can be done without problems.

The simulation of this algorithm was performed using the PYTHIA event generator with

an average of three minimum bias interactions per event. For B events, those minimum bias interactions were superimposed. All particles were followed through the silicon vertex detector including multiple scattering and photon conversion. The energy deposition in the pixels was computed and all the pixels with an energy deposit above a given threshold generated a hit. The hit information was then analysed as discussed above.

Figure 10 shows the normalised distributions of both $N_{\rm si}$ and Σ for minimum bias events and B$\rightarrow \pi^+\pi^-$ events. We also show Σ for those events which have survived after all the reconstruction cuts as well. The reconstruction cuts are listed elsewhere [5]. We request also a reconstructed lepton with a $p_{\rm T}$ larger than 1 GeV or a reconstructed kaon with an impact parameter larger than 100 μm for tagging.

Only $N_{\rm si}$ has been used in the first level trigger so far. As seen from figure 10, a better rejection of minimum bias events with the same efficiency for B events could be achieved by including the parameter Σ. Figure 10 also shows that an optimal first level trigger should match to the event reconstruction criteria. Then stronger trigger conditions could be used without losing many of the useful events. This study has not been undertaken yet. No attempt has been made to actually reconstruct secondary vertices in the first level trigger which needs also a further study.

When the optical discriminator is combined with the silicon trigger detector, the minimum bias reduction is always found to be about a factor 2 lower than the product of the individual reduction factors of the two components. There exist many possible choices of $N_{\rm ph}$, the threshold of the number of photoelectrons detected by the optical discriminator, and $N_{\rm si}$ or Σ which lead to the same minimum bias rejection factor. Figure 11 shows the efficiency for B$\rightarrow \pi^+\pi^-$ events as a function of the minimum bias rejection factor for different choices of the thresholds. The values scatter around a some sort of universal smooth curve. It is seen that one can easily achieve a combined rejection factor of ~ 30 keeping an efficiency of $\sim 45\%$ for B$\rightarrow \pi^+\pi^-$ events.

It is also worth noting that the optical discriminator has a good angular overlap with the silicon system I, but almost no angular overlapping with system II. This could call for more sophisticated combinations of the two impact parameter trigger components.

4.2 Large $p_{\rm T}$ trigger

The selection of events with a large $p_{\rm T}$ electron or hadron tracks is performed by an electromagnetic calorimeter (Ecal) and a hadronic calorimeter (Hcal) of moderate energy and spatial resolution but with fine granularity (40×40 mm^2 at small angles and increasing with the polar angle) and with fast charge collection. The online identification of γ, electron and hadron is performed by a pre-shower detector including two planes of scintillators S1 and S2 separated by 2 radiation lengths of lead. The pre-shower also gives the position of the particle. The arrangement is shown in figure 12.

A cluster energy is determined by summing up 3×3 towers in the Ecal and 7×7 towers in the Hcal. The $p_{\rm T}$ of each cluster is calculated according to its position and energy ignoring the magnetic deflection.

Each tile in the S1 and S2 planes has a low threshold discriminator to recognize minimum ionising particles. Those in S2 have also a higher discriminator threshold set well above the minimum ionisation energy deposition to recognize the beginning of an electromagnetic shower.

The $p_{\rm T}$ of the particle entering S1 in tile n is given by the $p_{\rm T}$ of the cluster centred on tile n. The type of the particle is given by the combination of the signals from the discriminators with low thresholds in S1 and S2 and the high threshold in S2; i.e. S1-low and S2-low for hadron, S1-low and S2-high for electron and no S1 and S2-high for γ.

The simulation of this arrangement included photon conversions, propagation of the charged particles through the magnetic spectrometer with multiple scattering, determination of the ionisation charge in S1, photon conversion and electron radiation in the pre-shower converter followed by the determination of the energy deposition in S2. Energy depositions in the Ecal and Hcal towers were calculated using standard shower profiles algorithms. The effect of pileup was taken into account with a simple model of charge collection time.

Those particles which penetrate the iron filter behind the hadronic calorimeter were identified as muons. Assuming that these particles came from an origin close to the target, their momenta and transverse momenta can be calculated from their positions and directions behind the filter alone. The simulation takes into account multiple scattering and pion and kaon decays. Pion punch-through was found to be negligible and omitted.

Figure 13 shows the p_T distributions of the electron and muon candidate with the highest p_T for B$\rightarrow$ J/ψK$_S$ events with J/$\psi \rightarrow e^+e^-$ and J/$\psi \rightarrow \mu^+\mu^-$. It also shows the p_T distribution of the p_T of the hadron candidate with the highest p_T for B$\rightarrow \pi^+\pi^-$ events. In each figure, the corresponding distribution for minimum bias events is also given. For minimum bias events, the distribution at large p_T arises mainly from conversion in the case of electrons and from pions and kaons decays in the case of muons. Table 1 gives an example for the trigger efficiencies for the B$\rightarrow$ J/ψK$_S$, for the B$\rightarrow \pi^+\pi^-$ channels and for minimum bias events.

Table 1: Example of p_T trigger efficiencies.

Studied channel	p_T threshold	Accepted	Minimum bias events
B$\rightarrow$ J/ψK$_S$,J/$\psi \rightarrow \mu^+\mu^-$	1.0 GeV muon	0.95	0.040
B$\rightarrow$ J/ψK$_S$,J/$\psi \rightarrow e^+e^-$	1.5 GeV electron	0.90	0.015
B$\rightarrow \pi^+\pi^-$	3.0 Gev hadron	0.55	0.030

4.3 Combined first level trigger

No correlations have been found between the p_T trigger and the impact parameter trigger. Therefore the combined minimum bias events rejection factor is simply given by the product of the rejection factors of both components.

In table 2 we present two examples of the combined first level trigger. The first one is our standard trigger with a variant without the optical discriminator. The second example, with stronger requirements on the impact parameter part of the trigger, is appropriate for the self tagging decay mode B$\rightarrow$ DK*. The table also gives a variant of the trigger which does not use the optical discriminator. An event rate of 40 MHz for minimum bias can easily be reduced to approximately 20 KHz in both examples.

Not all the potential of the each trigger component is used and the presented combinations are far from being optimal. But these few examples already show that the GAJET trigger concept is flexible and robust, with redundancy and can be tuned depending on the running conditions.

Table 2: Examples of possible trigger combinations. The first five columns show the threshold values for N_{ph} (the number of photoelectrons), N_{si} (the number of large impact parameter tracks), P_{Te} (the highest p_T of electron), P_{Tm} (the highest p_T of muon) and P_{Th} (the highest p_T of hadron). An event is accepted if both impact parameter trigger conditions are fulfilled and at least one track, electron, muon or hadron has a P_T above threshold. The last column shows the efficiency for minimum bias events.

N_{ph}	N_{si}	P_{Te}	P_{Tm}	P_{Th}	Channel	Total efficiency	Minimum bias
6	2	1.5	1.0	3.0	B$\rightarrow \pi^+\pi^-$	3.1%	6.1×10^{-4}
	2	1.5	1.0	3.5	B$\rightarrow \pi^+\pi^-$	3.3%	5.0×10^{-4}
10	3	1.5	1.0	2.0	B$\rightarrow$ DK*	2.4%	5.0×10^{-4}
	3	1.5	1.0	2.4	B$\rightarrow$ DK*	2.4%	5.0×10^{-4}

5 Expected Physics Performance[3]

5.1 Simulation Program

Several assumptions used for the physics results presented in this paper are listed here for reference. Unless otherwise stated, the results are quoted for one year of running, defined as 10^7 seconds, with an average luminosity of 2×10^{33} cm^{-2}s^{-1} for a proton beam on a hydrogen gas target. The assumed luminous region had a width in both x and y (transverse to the beam direction) of 50 μm and a width in z (along the beam direction) of 1 mm. The transverse size was determined by the beam dimension, while the longitudinal size was due to the distribution of gas from the jet.

5.1.1 Detector Simulation

The simulated detector used was that described in section 3 and in the GAJET Letter of Intent [4]. The simulation included kaon and pion decays, multiple scattering, photon conversions and energy loss, but did not include nuclear interactions. The track finding and hit association in the vertex detector was done without using any information of which of the actual tracks gave the hits. The algorithm is therefore close to what would be used in a real experiment.

5.1.2 B Decays Branching Ratios

The total $b\bar{b}$ cross section was assumed to be 1 μb. The different B hadron species were assumed to be produced in the ratios [13]

$$B^+ : B^0 : B_s : \overline{\Lambda}_b = 0.40 : 0.40 : 0.12 : 0.08$$

The decay modes were fixed according to the values given in [13]. In addition, the following were assumed

$$\begin{aligned} Br(B^0 \to J/\psi K_S, J/\psi \to l^+l^-, K_S \to \pi^+\pi^-) &= 3 \times 10^{-5} \\ Br(B^0 \to D^0_{CP=+1}K^{*0}, D^0_{CP=+1} \to \pi^+\pi^- \text{ or } K^+K^-, K^{*0} \to K^+\pi^-) &= 8 \times 10^{-8} \\ Br(B_s \to D_s^-\pi^+, D_s^- \to K^+K^-\pi^-) &= 2 \times 10^{-4} \end{aligned}$$

5.2 Measuring α Using $B^0 \to \pi^+\pi^-$

The basic technique of the CP-violation measurement reported here was to fit the proper time dependence of the partial decay rates of the particle or antiparticle decaying to a CP eigenstate. The measurement was therefore of a CP asymmetry where many uncertainties become small.

5.2.1 Expected Error

In the absence of background in the reconstructed B$\to \pi^+\pi^-$ signal and of any theoretical error (for α, a penguin contribution) the expected error on $\sin 2\alpha$ is [4]

$$\sigma_{\sin 2\alpha} = \frac{1}{(1-2\overline{\omega})I\sqrt{\epsilon N}}$$

where ϵ is the total efficiency for reconstructing the relevant channel (selection and tag), I is the statistical information of the data, $\overline{\omega}$ is the fraction of wrongly identified B^0 or $\overline{B}^0$ ("wrong tags") and N is the total number of $B^0 \to \pi^+\pi^-$ events. With the presence of the background, this error is increased by $\sqrt{1+R_{bg}}$ where R_{bg} is the ratio of background/signal in the selected sample.

[3] Presented by P. D. Dauncey

5.2.2 Selection of Events

The cuts for selecting $B^0 \to \pi^+\pi^-$ candidates are listed in [5]. They result in a selection efficiency of 3.1%. Figure 14 shows the resolution along the beam axis of the reconstructed vertices of these events. The width is 0.54 mm, which should be compared with the gas jet size of 1 mm which is used as the resolution for the primary vertex. No attempt was made to actually reconstruct the primary vertex. The resulting proper decay time resolution is shown in figure 15, which shows the proper time is measured to 4%.

Figure 16 shows the distribution of true decay times of $B^0 \to \pi^+\pi^-$ events, for all events, events which triggered and events which passed the selection criteria. It is seen that both the trigger and the selection remove a higher proportion of low lifetime events.

However, these events carry less information for the CP violation measurement as, roughly speaking, short lifetimes have not had time to mix. More quantitatively, figure 17 shows how the final error on $\sin 2\alpha$ depends on the effective lifetime cut, $\tau_{\rm min}$. Although the statistics are reduced sharply as this cut is increased, the remaining events have more weight, so the amount of information per event is greater (I value increases). For example, the effective cut around 1 ps gives a degradation in the result of only $\sim 5\%$.

5.2.3 Selection of Tag

To estimate the flavour of the b quark at the creation time, the charge of the opposite B hadron was determined using a charged lepton or kaon tag. The selection cuts are listed in [5] and result in a tag efficiency of 45% (21% from leptons and 24% from kaons), with a wrong tag ratio, $\overline{\omega}$, of 32% (25% for leptons, 38% for kaons). The main discriminator for lepton tags is the transverse momentum, $p_{\rm T}$. Figure 18 shows the $p_{\rm T}$ spectrum for right-signed and wrong-signed leptons. A clear separation between the two is observed. Figure 19 shows the true decay time of the B hadrons producing the lepton tags; the reduction at small decay times due to the trigger is again observable, but no further reduction from the lepton selection is seen (the lepton $p_{\rm T}$ cuts do not depend on the vertex position). In contrast to the signal selection, removing small lifetime events for the tag is undesirable, as these B hadrons will have mixed less and so are more likely to identify correctly the sign of the b quark. Unfortunately, the kaon tags are mainly discriminated from background by their impact parameters, shown for right-sign and wrong-sign in figure 20. The resulting true decay times, figure 21, show a corresponding reduction of short lifetime tag events from the impact parameter cut. This is one of the main reasons why the kaon tag has a worse wrong tag rate than the lepton tag.

5.2.4 Backgrounds

The main backgrounds to the $B^0 \to \pi^+\pi^-$ sample were from other B decays into two charged particles and random combinations of tracks forming fake vertices in $b\overline{b}$ events. Minimum bias, $c\overline{c}$ and $b\overline{b}$ (with the two candidate tracks from the same B hadron) were found to give negligible backgrounds. Eight different exclusive background channels were studied [13]. These gave a total contribution equal to 20% of the signal, of which the majority (12%) was from $B^0 \to K^+\pi^-$, where the kaon was misidentified. For the random combinations, 1.8 million generated $b\overline{b}$ events gave three events passing the selection criteria. Scaling this to the assumed $B^0 \to \pi^+\pi^-$ branching ratio (section 5.1) gave a background from this source equal to 10% of the signal, or a total background/signal ratio, $R_{\rm bg}$, of 0.3. Figure 22 shows the expected signal and total background.

5.2.5 Systematics

Since the measurement is of a time-dependent CP asymmetry, many potential systematics cancel. For example, the dependence of the result on the assumed detector resolution of the decay time was studied [5] and found to be negligible. The biggest systematic effects would be likely to arise from the corrections necessary to extract the actual asymmetry from the experimentally measured

asymmetry. The most basic of these corrections would be needed because of the wrong tags; the real asymmetry, A, is related to the measured asymmetry, A', by

$$A = \frac{A'}{1 - 2\overline{\omega}}$$

so that an error on the wrong tag rate, $\overline{\omega}$, would directly give an error on A. The other corrections which would be applied arise because the initial state is pp not $p\overline{p}$, so that B^0 and $\overline{B}^0$ production would not necessarily be identical. In general, there would be differences in the rates for $\overline{b} \to B^0$ and $b \to \overline{B}^0$, the momentum spectra of the B^0 and $\overline{B}^0$, and also the tag efficiency and the wrong tag rate for B^0 and $\overline{B}^0$. These differences would have to be measured from the data directly, for which separate samples of B^0 and $\overline{B}^0$ would be required. One reaction which could be used to provide such samples is

$$B^0 \to J/\psi K^{*0}, K^{*0} \to K^+\pi^-$$

$$\overline{B}^0 \to J/\psi \overline{K}^{*0}, \overline{K}^{*0} \to K^-\pi^+$$

where the sign of the kaon and pion of the K^* decay would give the type of B meson. Note the systematic corrections calculated from these samples would be statistics limited.

5.2.6 Results for α

Assuming $\sigma_{b\overline{b}} = 1\ \mu b$, $\mathcal{L} = 2 \times 10^{33}\ cm^{-2}s^{-1}$ and one year $= 10^7$ seconds, the numbers of events for this measurement are given in table 3.

Table 3: Numbers of events for $B^0 \to \pi^+\pi^-$ after one year of data taking.

Number of $b\overline{b}$ events	2.0×10^{10}
Number of $B^0, \overline{B}^0$ events	1.6×10^{10}
Number of $B^0, \overline{B}^0 \to \pi^+\pi^-$ events	3.2×10^5
Number reconstructed	9.9×10^3
Number reconstructed with tags	4.5×10^3

If there is no penguin contribution [14], then the error on $\sin 2\alpha$ after one year of data taking would be

$$\sigma_{\sin 2\alpha} = 0.041 \pm 0.023 \pm 0.018$$

where the quoted errors are due to statistics, background and systematics respectively. All these errors would scale as $1/\sqrt{N}$. The total error would therefore be

$$\sigma_{\sin 2\alpha} = 0.051$$

This result is sensitive to the penguin contribution and the level to which the contribution is measured. If the penguin contribution were known to $\pm 20\%$ for example [13], then (assuming $\delta_0 = \delta_2 = 45°$), the error would increase to [5]

$$\sigma_{\sin 2\alpha} = 0.090$$

Finally, the effect of not using kaon tags was investigated. Because the kaon tags have a larger wrong tag rate, they do not have a great weight in the result. If only lepton tags were used, the error would only increase to

$$\sigma_{\sin 2\alpha} = 0.056$$

5.3 Measuring β Using $B^0 \to J/\psi K_S$

The measurement of the CP violation parameter β has been studied using the decay $B^0 \to J/\psi K_S$, where $J/\psi \to l^+l^-$ (l = e or μ) and $K_S \to \pi^+\pi^-$. Again, the event selection is described in [4] and has an efficiency of 3.2% for $J/\psi \to \mu^+\mu^-$. However, because electrons would radiate as they pass through the material of the detector, they would lose a significant amount of energy. The resulting J/ψ reconstructed mass peak is shown in figure 23, where the long tail on the low side is clearly visible. The efficiency for the channel $J/\psi \to e^+e^-$ would be only 1.6% because of this effect. The mass peaks for the J/ψ, K_S and B^0 obtained are shown in figures 24, 25 and 26. The final B^0 mass resolution was 24 MeV. The tag selection, efficiencies and wrong tag rates were effectively the same as for the measurement of α (section 5.2). The background was found to be at most 50% of the signal.

5.3.1 Results for β

Assuming $\sigma_{b\bar{b}} = 1$ μb, $\mathcal{L} = 2 \times 10^{33}$ cm^{-2}s^{-1} and one year $= 10^7$ seconds, the numbers of events for this measurement are given in table 4.

Table 4: Numbers of events for $B^0 \to J/\psi K_S$ after one year of data taking.

Number of $b\bar{b}$ events	2.0×10^{10}
Number of $B^0, \overline{B}^0$ events	1.6×10^{10}
Number of usable $B^0, \overline{B}^0 \to J/\psi K_S$ events	4.8×10^5
Number reconstructed	2.3×10^4
Number reconstructed with tags	9.4×10^3

The error on $\sin 2\beta$ after one year of data would be

$$\sigma_{\sin 2\beta} = 0.032 \pm 0.023 \pm 0.018$$

where again the errors are due to statistics, background and systematics respectively. All these errors would scale as $1/\sqrt{N}$. The total error would therefore be

$$\sigma_{\sin 2\beta} = 0.043$$

5.4 Measuring γ Using $B^0 \to D^0K^{*0}$

An equivalent method to measure γ to those used for α and β above would be to measure the time dependence of a reaction such as [15]

$$B_s \to \rho^0 K_S$$

measuring $\sin 2\gamma$ or

$$B_s \to D_s^- K^+$$

measuring $\sin \gamma$.

A different method [16, 17] is to measure the CP violation parameter, γ, from the six rates of B^0 decaying into D^0K^{*0}, $\overline{D}^0K^{*0}$ and $D^0_{CP}K^{*0}$ and $\overline{B}^0$ into $D^0\overline{K}^{*0}$, $\overline{D}^0\overline{K}^{*0}$ and $D^0_{CP}\overline{K}^{*0}$. D^0_{CP} decays to a CP=$\pm$1 state. Useable examples of such states are $D^0_{CP} \to \pi^+\pi^-$ or K^+K^- for CP=+1 states and $D^0_{CP} \to \rho^0 K_S$ or ϕK_S for CP=$-$1 states. Note, in addition, charged $B^\pm$ decays could be used to increase the statistics.

Again, the event selection is described in [5] and was found to have an efficiency of 2.4%.

5.4.1 Results for γ

Assuming $\sigma_{b\bar{b}} = 1\ \mu b$, $\mathcal{L} = 2 \times 10^{33}\ cm^{-2}s^{-1}$ and one year $= 10^7$ seconds, the numbers of events for this measurement are given in table 5.

Table 5: Numbers of events for the self tagging mode used to measure $\sin 2\gamma$ after one year of data taking.

Number of $b\bar{b}$ events	2.0×10^{10}
Number of B^0 events	8×10^9
Number of usable $B^0 \to D^0 K^{*0}$ events	2.0×10^3
Number reconstructed $B^0 \to D^0 K^{*0}$ events	4.8×10^1
Number of usable $B^0 \to \overline{D}^0 K^{*0}$ events	6.0×10^3
Number reconstructed $B^0 \to \overline{D}^0 K^{*0}$ events	1.4×10^2
Number of usable $B^0 D^0_{CP=+1} \to K^{*0}$ events	6.7×10^2
Number reconstructed $B^0 \to D^0_{CP=+1} K^{*0}$ events	1.6×10^1

The resulting error on γ would be much larger than for α or β as the measurement would be severely limited by the statistics of the D^0_{CP} decays. This depends on the strong phase, Δ, between $B \to \overline{D}K$ and $B \to DK$. For the maximal rate of D^0_{CP} decays, $\Delta = 90°$ and the resulting error on $\sin 2\gamma$ after one year of data would be

$$\sigma_{\sin 2\gamma} = 0.21$$

where the error is statistical only. For more pessimistic assumptions on Δ, $\Delta = 60°$ or $30°$ for example, then the error would become

$$\sigma_{\sin 2\gamma} = 0.31, 0.69$$

respectively. Again these would all scale as $1/\sqrt{N}$.

Note that in the measurements of sections 5.2 and 5.3, the main systematic resulted from the limitation of the knowledge on differences in B and $\overline{B}$. Here, the decay is self-tagging, so no tag was required. Therefore, the systematics would be very different and would be expected to be small compared with the above statistical error, even after several years of data taking.

A study done after this conference [3] shows that the GAJET detector can measure $\sin\gamma$ after one year of data taking with

$$\sigma_{\sin\gamma} = 0.17\ (0.42)$$

for

$$x_s = 10\ (30)$$

using $B_s \to D_s^- K^+$.

5.5 Measurement of B_s Oscillations Using $B_s \to D_s^- \pi^+$

The reaction

$$B_s \to D_s^- \pi^+, D_s^- \to K^+ K^- \pi^-$$

was studied to measure B_s mixing. The event selection is described in [5] and has an efficiency of 3.9%. The tag results were effectively the same as above (section 5.2). Figure 27 shows the B_s invariant mass, which has a width of 35 MeV, and the contribution from one of the background channels considered

$$B_s \to D_s^{*-} \pi^+, D_s^{*-} \to D_s^- \gamma$$

where the photon is lost. It is seen that the mass resolution would be sufficient so that rejection of this background would be straightforward. Again, similar to the case for $B^0 \to \pi^+\pi^-$, the decay length error would be dominated by the gas jet size and so the resulting proper time resolution would be similar, 4%. Figure 28 shows an example of the observed asymmetry obtained for $x_s = 30$ where the oscillations are clearly seen. The oscillations folded by the correct time period are shown in figure 29 for x_s of 30, 50 and 75. It is seen that for $x_s = 50$ or above, the asymmetry would become difficult to observe. An upper limit on x_s of 45 was estimated using this method.

5.5.1 Results for x_s

Assuming $\sigma_{b\bar{b}} = 1$ μb, $\mathcal{L} = 2 \times 10^{33}$ cm^{-2}s^{-1} and one year $= 10^7$ seconds, the numbers of events for this measurement are given in table 6.

Table 6: Numbers of events for $B_s \to D_s^-\pi^+$ after one year of data taking.

Number of $b\bar{b}$ events	2.0×10^{10}
Number of $B_s, \overline{B}_s$ events	4.8×10^9
Number of usable $B_s, \overline{B}_s \to D_s^-\pi^+$ events	1.1×10^6
Number reconstructed	4.3×10^4
Number reconstructed with tags	1.9×10^4

The value of x_s extracted from a fit to the number of events expected from one year of data taking gave

$$x_s = 45.03 \pm 0.08$$

for an input value of $x_s = 45$. Hence, the statistical error would be expected to be $\sim 0.2\%$. Systematics from uncertainties in the background, resolution and tag rates have been studied and give a negligible effect on the measured period of oscillation. The most important systematic may result from the uncertainty in the absolute length (or momentum) scale of the detector. To be small compared with the above statistical error, this scale would have to be known to $\sim \pm 0.1\%$, which, for example, would require the B_s mass to be known to ± 50 MeV. It is hoped that such an error on the detector scale could be obtained by careful calibration of the tracking to particles with accurately known masses (J/ψ, Υ and $B_{u,d}$).

5.6 Limits on Rare B Decays

Two examples of searches for rare B decays are reported here.

5.6.1 $B_s \to \mu^+\mu^-$

The selection for this channel was almost identical to that for $B^0 \to \pi^+\pi^-$ [5], with an additional cut on the muon identification. The efficiency for the selection was 2.7%. The main background was found to arise from $B \to l^+X$, $\overline{B} \to l^-X$, which was estimated to give 120 events/year. Hence, the 95% confidence level (CL) cut on $B_s \to \mu^+\mu^-$ would be for 25 events/year, so after one year, the 95% CL upper limit on the branching ratio would be

$$Br(B_s \to \mu^+\mu^-) < 2 \times 10^{-7}$$

The expected Standard Model branching ratio [18] is 1.8×10^{-9}, so no signal would be expected without new physics [4].

[4] A more detailed study has been done [3] since the conference, giving an improved limit of $Br(B_s \to \mu^+\mu^-) < 1 \times 10^{-7}$. However, the above conclusion still holds.

5.6.2 $B^0 \to K^{*0}\mu^+\mu^-$

This is similar to the above, but the additional requirement for a K^{*0} reduced the efficiency to 1.5% with a background of 260 events/year. Because the B^0 was assumed to be produced more frequently than the B_s, the limit does not degrade as badly as might otherwise be expected; the resulting 95% CL limit was

$$Br(B^0 \to K^{*0}\mu^+\mu^-) < 5 \times 10^{-7}$$

In this case, the Standard Model branching ratio [18] is 2.9×10^{-6}. Hence, this measurement would be expected to either see a signal or place a limit which is not compatible with the Standard Model.

6 Summary and Conclusions

GAJET could run from the first day of operation of the LHC to do CP violation physics. The choice of hydrogen or argon gas would allow a wide range of beam intensities to be used. In addition, the GAJET trigger scheme, comprising high-p_T triggers and two separate lifetime triggers, would be flexible enough to deal with varying beam conditions and would have a lot of redundancy.

GAJET would not be a difficult detector to build. The requirements for the gas jet, most detector components and the LHC itself would be relatively conservative. In particular, the point-like target would make the lifetime trigger very much easier technically.

Acknowledgement

The results presented here were produced by the members of the GAJET collaboration. The authors would like to thank the organising committee, in particular P. Schlein and Y. Lemoigne for the success of this workshop.

References

[1] See contributions from various experiments in these proceedings.

[2] I. I. Bigi et al., in "CP Violation", edt. C. Jarlskog, World Scientific, Singapore, 1989
Theoretical discussions are also given by I. Bigi and D. Wyler in these proceedings.

[3] GAJET Collaboration, "Additional Comments to the LHCC Questions", CERN/LHCC 94-24, 1994.

[4] GAJET Collaboration, Letter of Intent, CERN/LHCC 93-54, 1993.

[5] GAJET collaboration, "Reply to The LHCC Questions", CERN/LHCC 94-13, 1994.

[6] This technique was pioneered by P238
J. Ellett et al., Nucl. Instr. Methods **A317** (1992) 28.

[7] G. Charpak, Y. Giomataris and L. Lederman, Nucl. Instr. Methods **A306** (1991) 439.

[8] G. Charpak et al., Nucl. Instr. Methods **A332** (1993) 91.

[9] D.M. Kaplan et al., Nucl. Instr. Methods **A330** (1993) 33.

[10] G. Charpak et al., "Study of an Optical Trigger to be used for Beauty search in fixed target mode at LHC", CERN-DRDC/RD30, 1991.

[11] See the contribution of C. Kochowski in these proceedings.

[12] M. Atac et al., Nucl. Instrum. Methods **A314** (1992) 56-62.

[13] LHCC Committee, "Referees' questions for the B-experiments", CERN/LHCC 94-3 (1994).

[14] See [2] for further references.

[15] I.I. Bigi et al in [2]
R. Aleksan et al., Z. Phys. **C54** (1992) 653.

[16] M. Gronau and D. Wyler, Phys. Lett. **B265** (1991) 172.

[17] I. Dunietz, Phys. Lett. **B270** (1991) 75.

[18] A. Ali, CERN-TH 7168/94 (1994) and these proceedings.

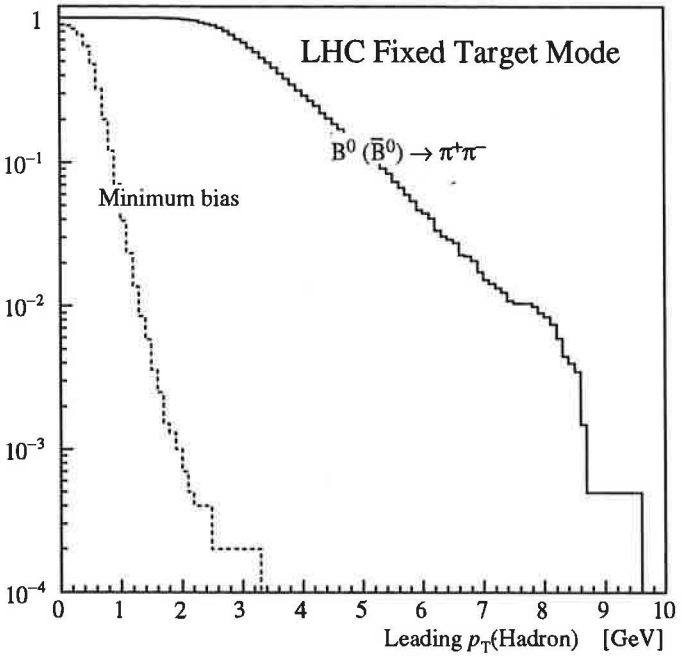

Figure 1: The p_T distribution, in fixed target mode, of the charged hadron with the highest p_T in the event, for minimum bias events and for $b\bar{b}$ events where one of the b quarks hadronises to a neutral B-meson which then decays into $\pi^+\pi^-$. The geometrical acceptance is limited in the polar angle to 3.5-87 mrad.

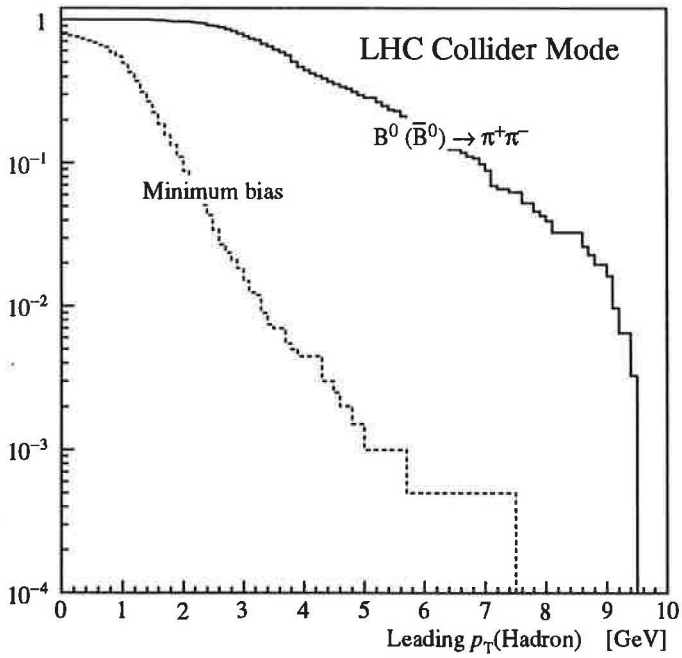

Figure 2: Same plot as above for collider mode. The geometrical acceptance is limited in the polar angle to 10-600 mrad.

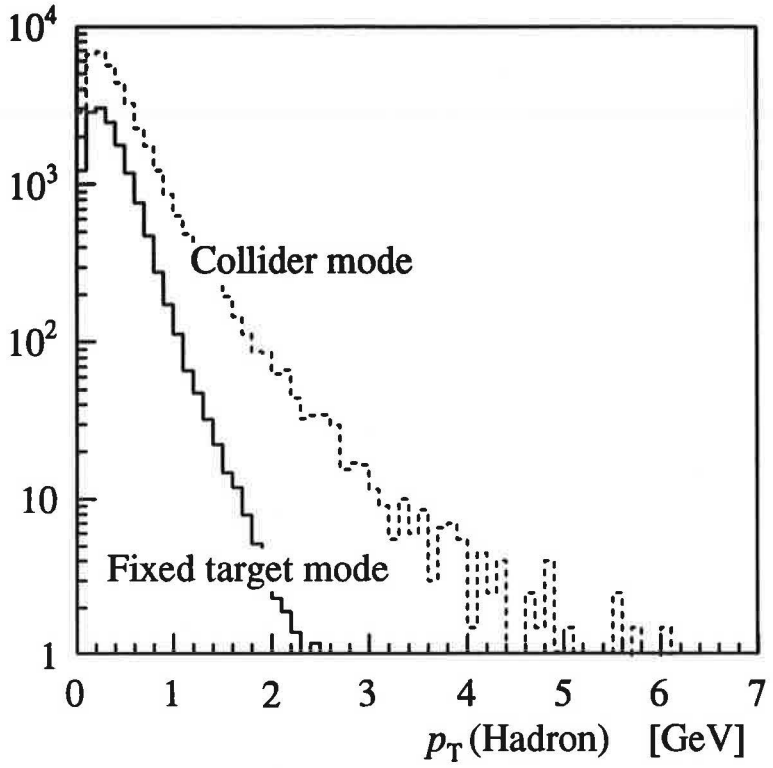

Figure 3: Transverse momentum distribution of hadrons produced in the minimum bias events for collider mode and fixed target mode.

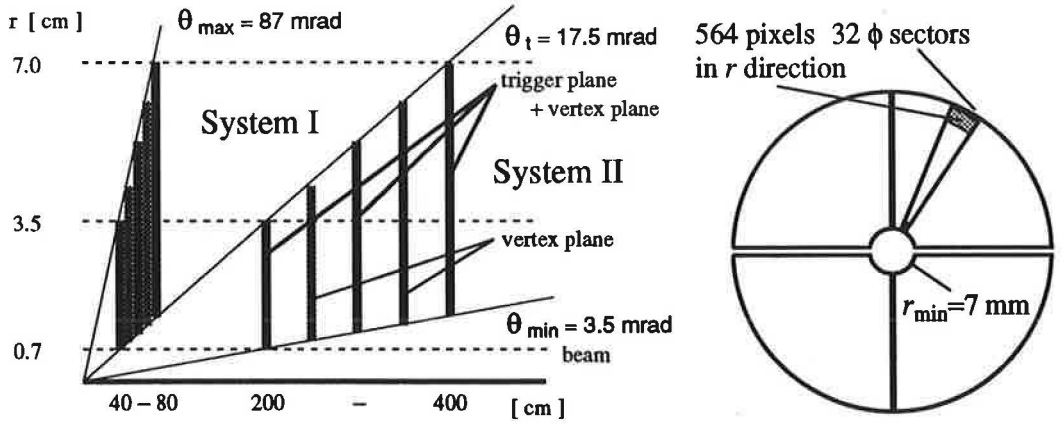

Figure 4: A vertex trigger system designed for an experiment having a point-like a priori known target.

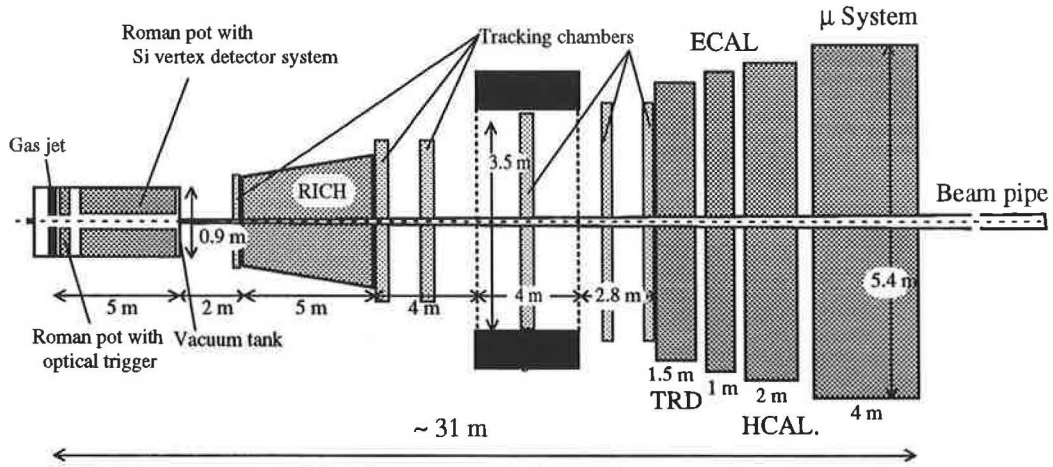

Figure 5: Overall schematic view of the GAJET detector.

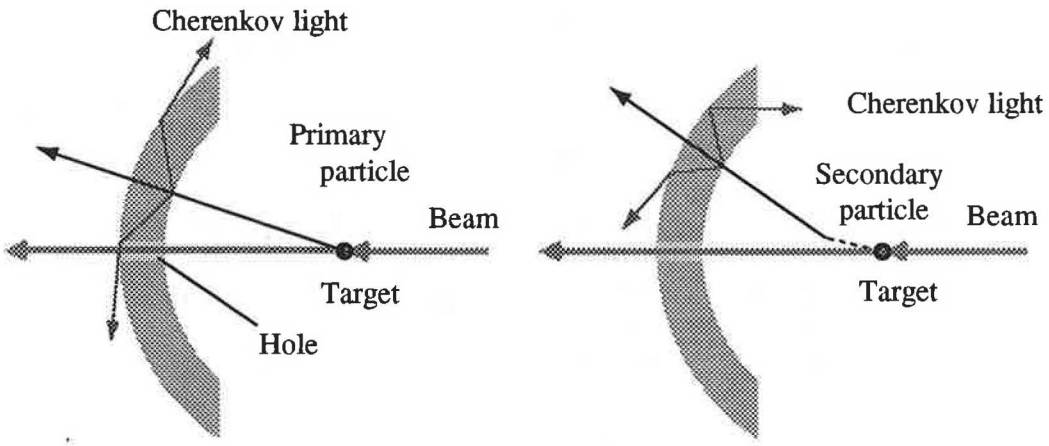

Figure 6: The principle of the optical discriminator.

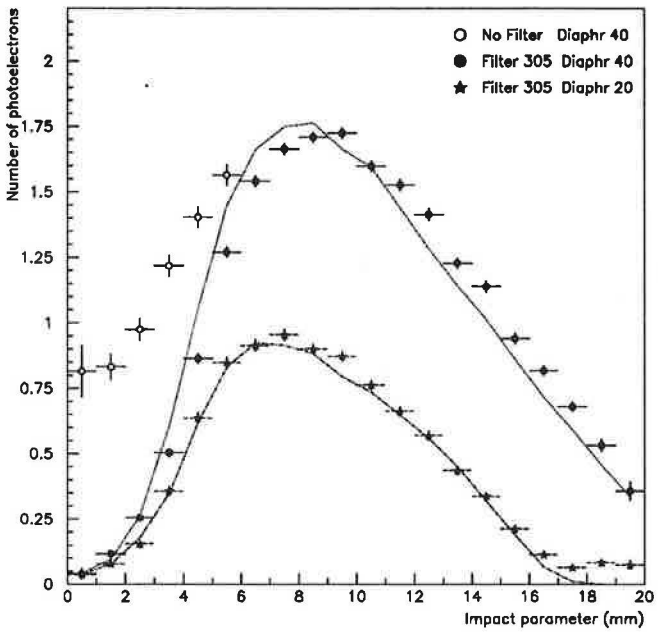

Figure 7: Results from RD30. The number of photoelectrons as a function of the impact parameter for a LiF crystal. The points are the data and the solid curve results from a simulation of the device.

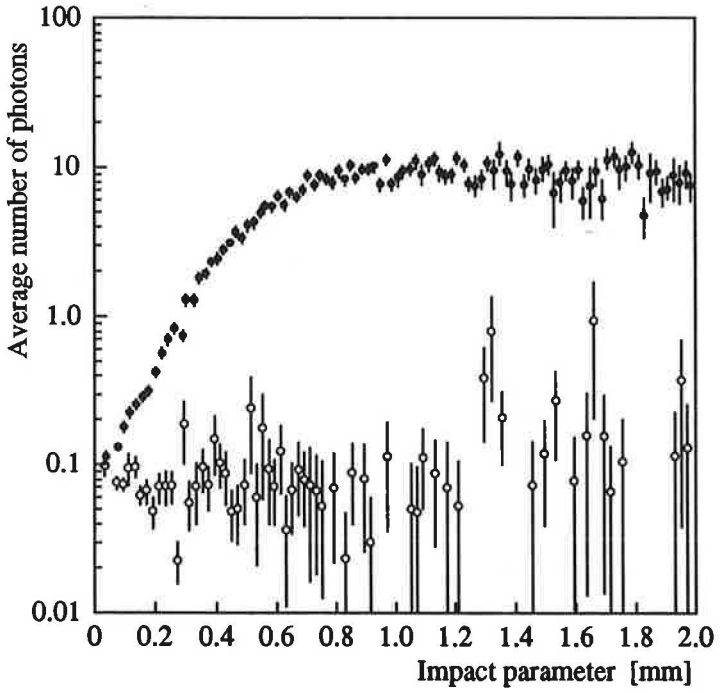

Figure 8: The number of photoelectrons per particle crossing the crystal as a function of the impact parameter for a six layer sapphire device with liquid cladding. The open circles are background.

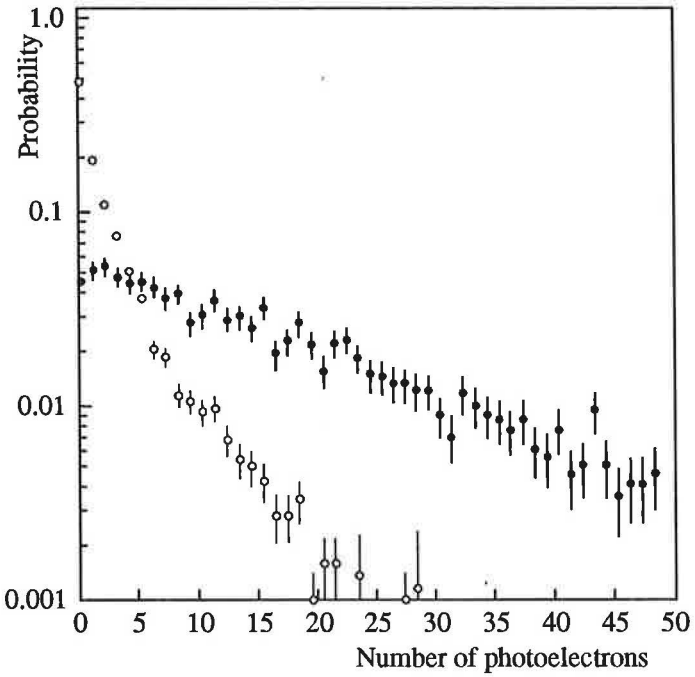

Figure 9: Normalised distributions of the number of photoelectrons for $B^0 \rightarrow \pi^+\pi^-$ events (closed circles) and for minimum bias events (open circles).

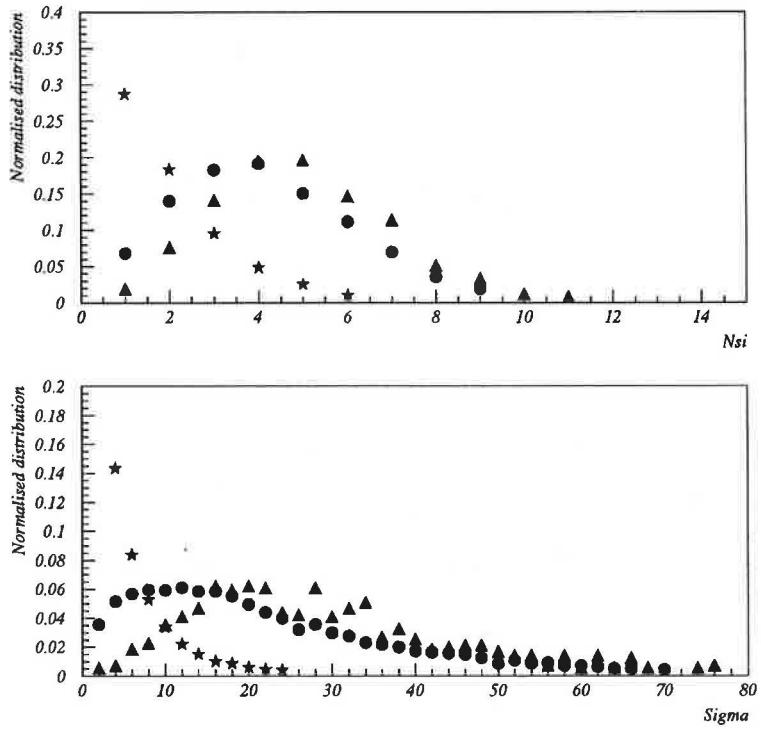

Figure 10: Normalised distributions of the parameters $N_{\rm si}$ (top) and Σ (bottom) (see text for dedinition) for all $B^0 \rightarrow \pi^+\pi^-$ events (dots), reconstructed and tagged (triangles) and for minimum bias events (stars).

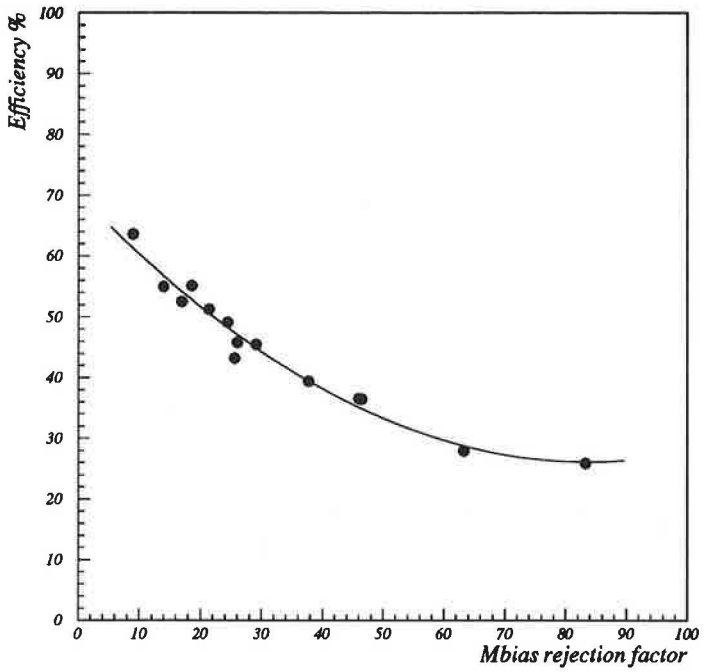

Figure 11: Variation of the efficiency for $B^0 \to \pi^+\pi^-$ events with the rejection factor for minimum bias events when the two impact parameter trigger components are combined.

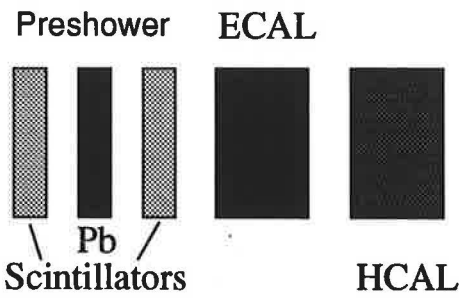

Figure 12: GAJET calorimeter arrangement.

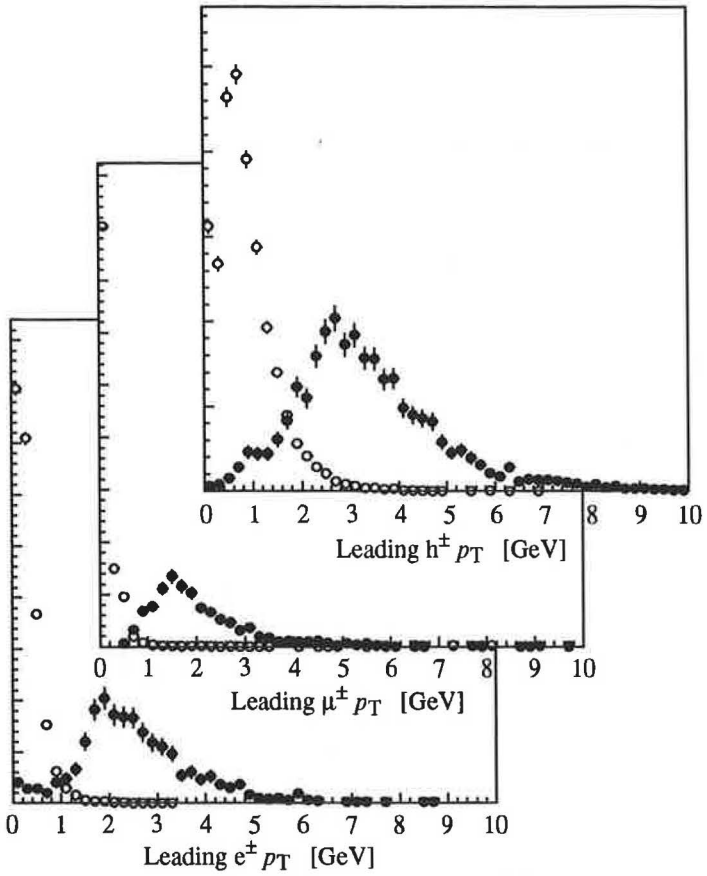

Figure 13: The measured p_T distributions of the leading electron and muon for B$\rightarrow$ J/ψK$_S$ (closed circles) and for minimum bias events (open circles). It also shows the measured p_T distributions of the leading hadron for B$\rightarrow$ $\pi^+\pi^-$ events (closed circles) and for minimum bias events (open circles).

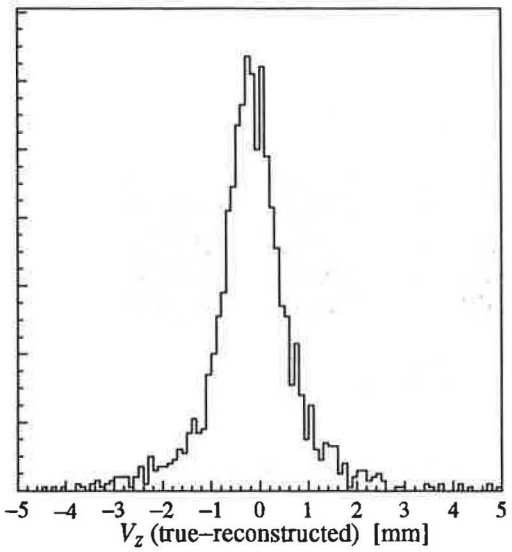

Figure 14: Reconstructed secondary vertex resolution for $B^0 \rightarrow \pi^+\pi^-$.

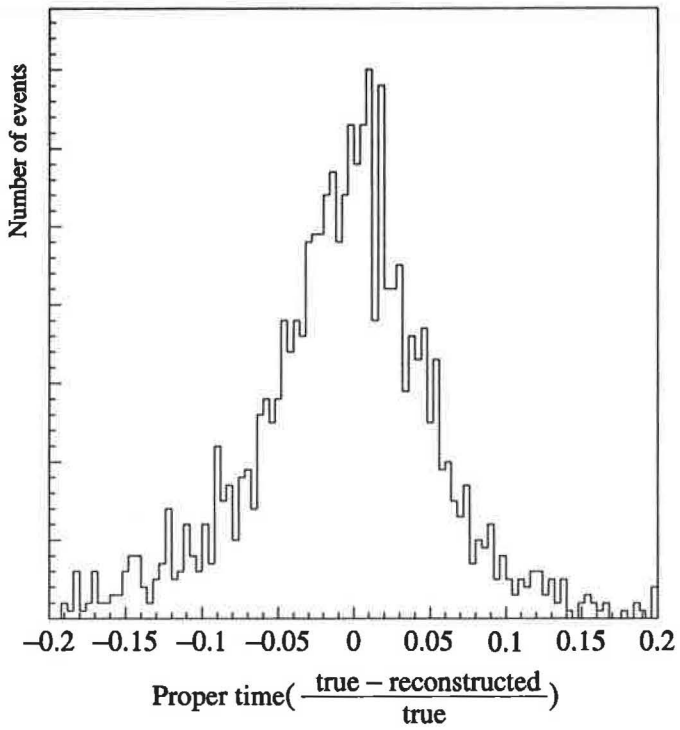

Figure 15: Relative proper time resolution for $B^0 \to \pi^+\pi^-$.

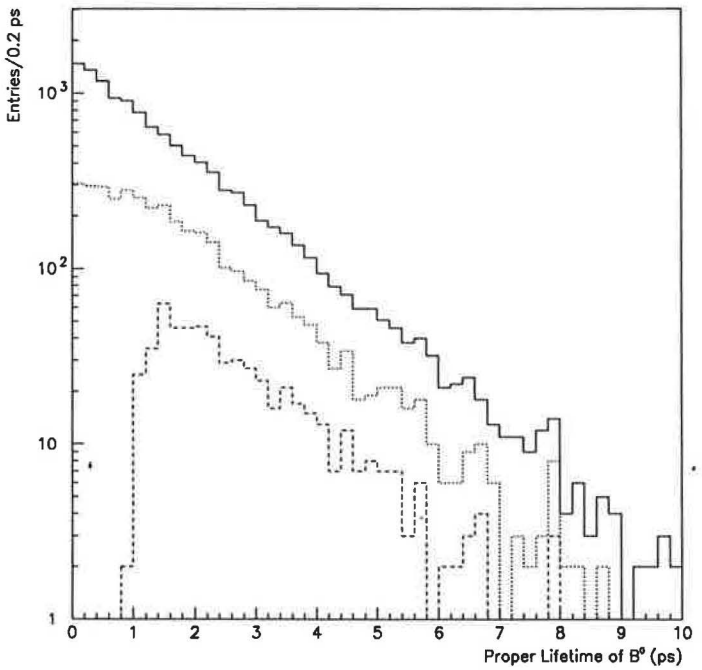

Figure 16: True proper time distribution for generated, triggered and reconstructed $B^0 \to \pi^+\pi^-$ decays.

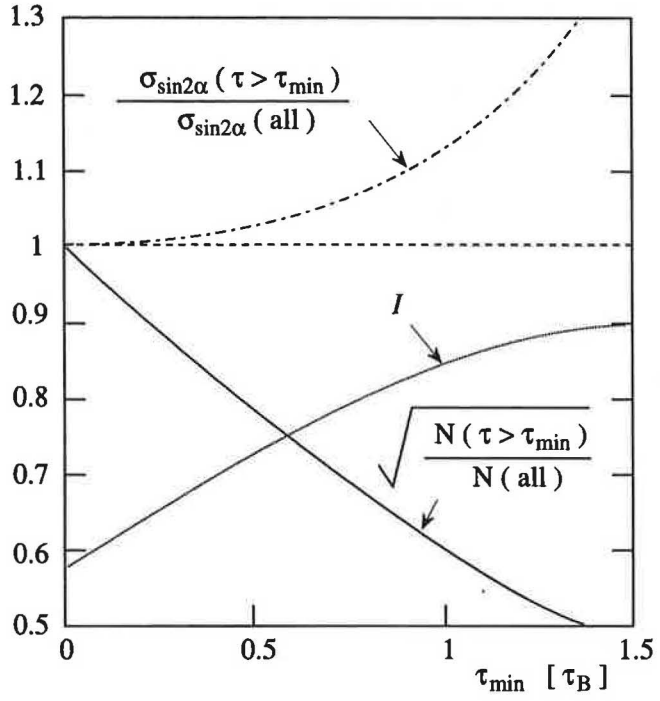

Figure 17: Relative CP sensitivities as a function of the cut applied on the minimum proper time.

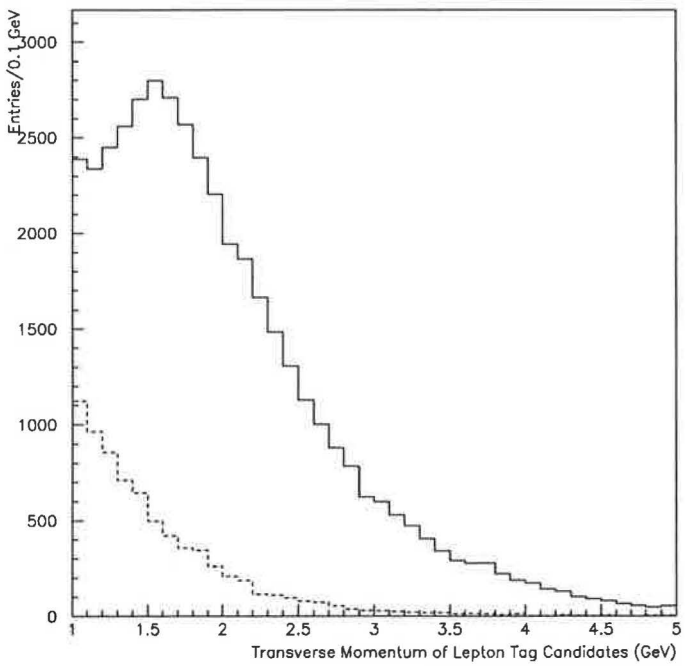

Figure 18: Measured transverse momentum spectra for candidate tag leptons with the right-sign tag (solid line) and wrong-sign tag (dashed line).

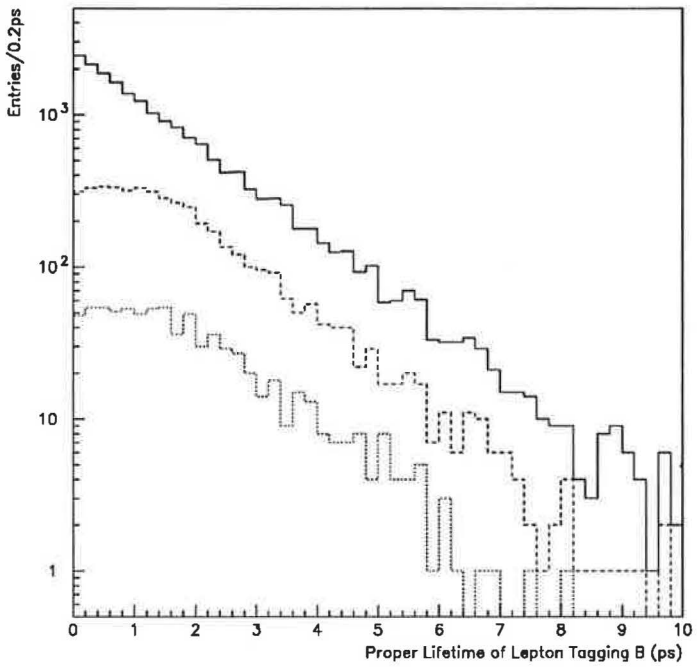

Figure 19: True proper time distribution of tagging B hadrons for generated, triggered and lepton-tagged decays.

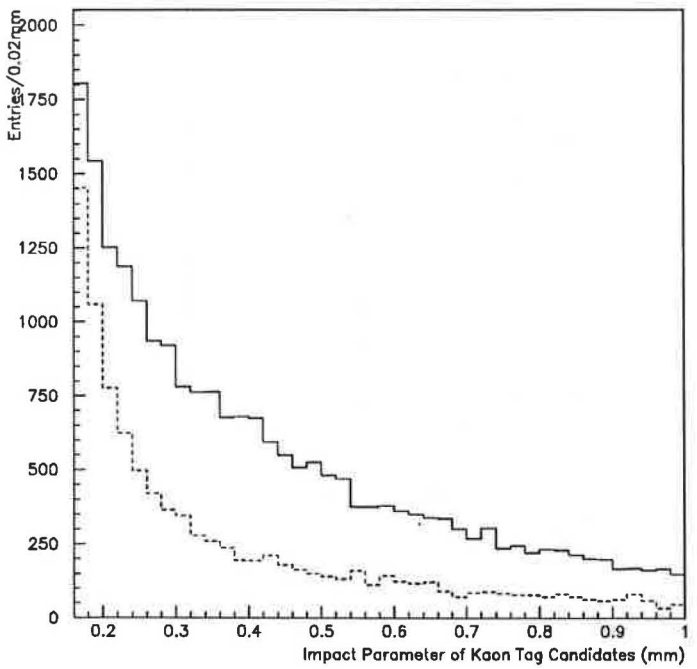

Figure 20: Measured impact parameter distributions for candidate tag kaons with the right-sign tag (solid line) and wrong-sign tag (dashed line).

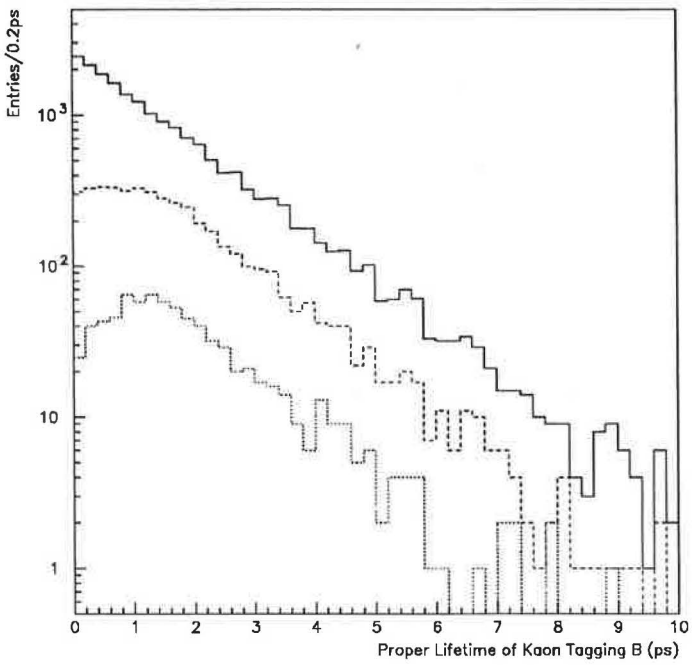

Figure 21: True proper time distribution of tagging B hadrons for generated, triggered and kaon-tagged decays.

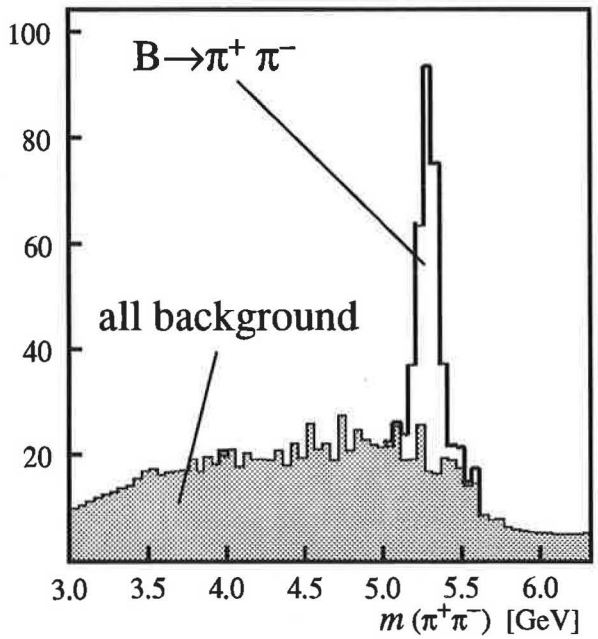

Figure 22: Invariant mass distribution of reconstructed $B^0 \rightarrow \pi^+\pi^-$ signal with all background (shaded region).

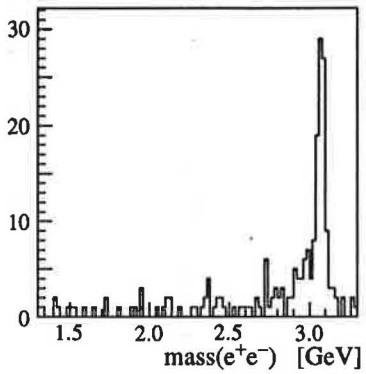

Figure 23: Reconstructed e^+e^- invariant mass distribution for J/ψ decays.

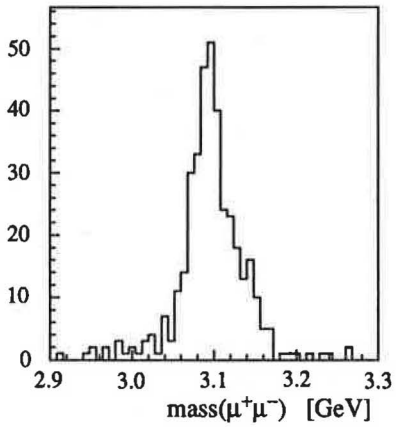

Figure 24: Reconstructed $\mu^+\mu^-$ invariant mass distribution for J/ψ decays. Note the change of scale relative to figure 23.

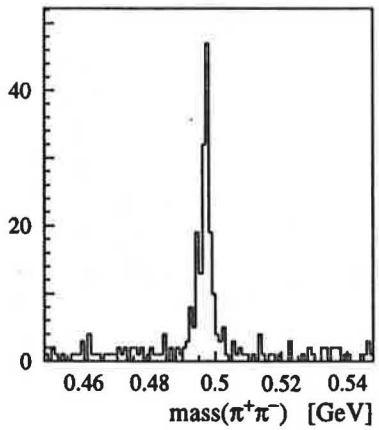

Figure 25: Reconstructed $\pi^+\pi^-$ invariant mass distribution for K_S decays.

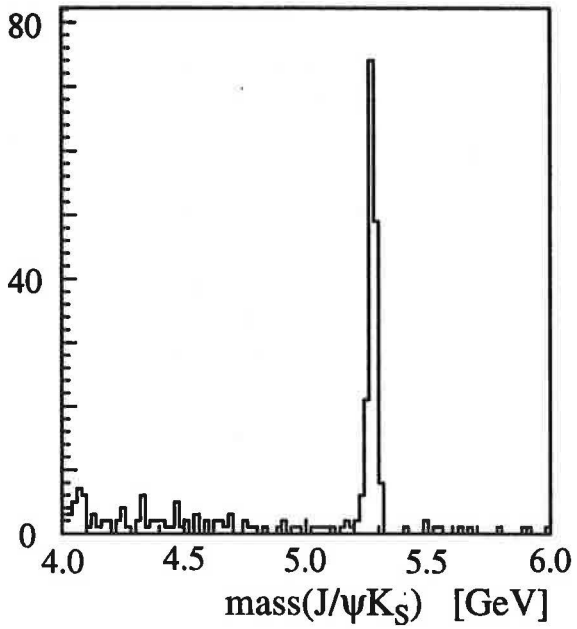

Figure 26: Reconstructed $J/\psi K_S$ invariant mass distribution for B^0 decays.

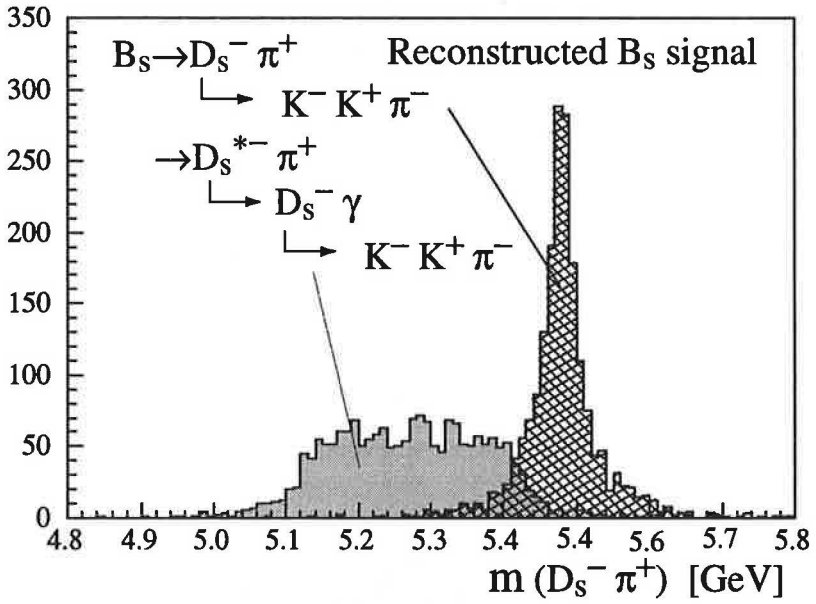

Figure 27: Reconstructed $D_s\pi$ invariant mass distribution for B_s decays.

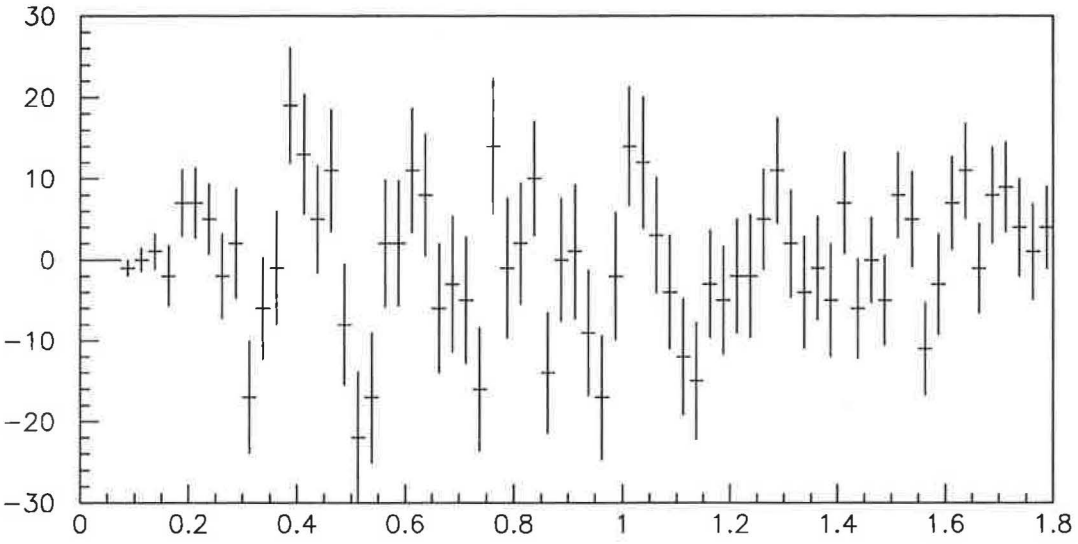

Figure 28: Observed decay rate difference in $B_s$decays for $x_s = 30$.

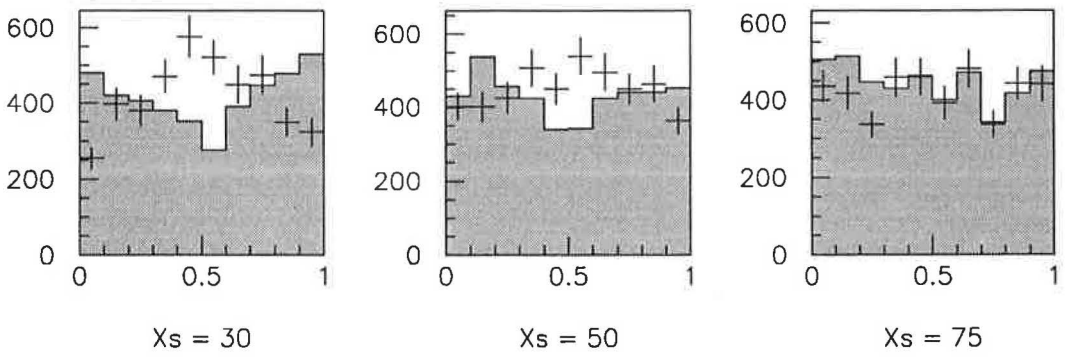

Figure 29: Reconstructed proper $B_s$decay time modulo the period $x_s t/2\pi$ for the same and opposite flavour tags for $x_s = 30$, 50 and 75.